Available online at www.sciencedirect.com
SCIENCE DIRECT®
Materials Chemistry and Physics 81 (2003) 11–26
MATERIALS CHEMISTRY AND PHYSICS
www.elsevier.com/locate/matchemphys

Review

Texture analysis in hexagonal materials

Y.N. Wang [a,b], J.C. Huang [a,*]

[a] *Institute of Materials Science and Engineering, National Sun Yat-Sen University, Kaohsiung, Taiwan 804, RO China*
[b] *Dalian University of Technology, Dalian 116024, PR China*

Received 18 June 2002; received in revised form 20 November 2002; accepted 26 November 2002

Abstract

Textures in the hexagonal metals have attracted significant interest over the years because of the use of some hexagonal metals and alloys, e.g. Zircaloy cladding for nuclear reactor fuels, Ti alloys for aerospace and aircraft industry, and Mg alloys for automobile and computer, communication and consumer electronic (3C) appliances. From a mechanistic point of view, hexagonal metals are different from cubic metals due to the restricted slip systems and the activation of twinning. In this paper, a brief summary of the texture in hexagonal structural materials is carried out, mainly dealing with the deformation and recrystallization texture as well as the anisotropy of textured hexagonal materials.

Keywords: Texture; Hexagonal materials; Pole figures; Orientation distribution function

1. Introduction

The properties of many crystalline materials depend on the individual properties of the single crystals and also on parameters characterizing the polycrystalline state. Since preferred orientations of the grains are very common phenomena, crystalline texture sometimes plays an important role in terms of numerous mechanical and physical behaviors. In literature, the preferred orientation is mainly classified into the "deformation texture" and "recrystallization (or annealing) texture". The texture may undergo evolution during casting, processing, deformation, welding, as well as heat treatment. When all possible orientations of the crystallites occur with equal frequency, the orientation dependence will disappear on the average, and the polycrystalline material thus behaves isotropically on average. However, complete isotropic characteristics are difficult to achieve since a certain level of mechanical fibering tends to occur in most deformed materials, inducing orientation dependence. A typical instance is the sheet metals used for deep drawing; the semi-isotropic characteristic is required in order to avoid undesirable earing. On the other hand, if all crystals are nearly similarly oriented, the behavior of the polycrystalline material in many respects resembles that of a single crystal. A prominent example of this case is the so-called "cube texture" in cubic crystal metals. In that case, all grains are oriented so that the $\{0\,0\,1\}$ planes lie nearly parallel to the plane of the sheet and the $\langle 1\,0\,0\rangle$ directions point approximately in the rolling direction. This texture ($\{0\,0\,1\}\langle 1\,0\,0\rangle$) and Goss texture ($\{1\,1\,0\}\langle 0\,0\,1\rangle$) are usually desired in magnetic materials, in which it is easy to magnetize in the cube edge $\langle 1\,0\,0\rangle$ direction.

There are many typical texture components simultaneously present in polycrystalline materials, so that the texture distribution is of concern. By now, the pole figures or inverse pole figures are most frequently used to characterize the texture in polycrystalline materials by using X-ray diffraction, although there are some limitations due to the two-dimensional information for three-dimensional crystallographic spaces. Orientation distribution function (ODF) is another tool that is much more precise in terms of the presentation for individual texture components. Meanwhile, there are other newly developed methods favorable for micro-texture analyses on small local regions, such as the electron back-scattered diffraction (EBSD) in association with scanning electron microscopy (SEM) [1–4], or the rapid analysis of electron diffraction patterns taken from each of the viewed grains by transmission electron microscopy (TEM) [5,6]. A number of commercial or private software programs are available worldwide.

Texture in hexagonal structural materials have attracted significant interest over the years because of the use of zirconium alloys Zircaloy for cladding of nuclear reactor fuels [7,8], titanium alloys for structural materials in aerospace and aircraft industry [9–16], as well as magnesium alloys as

* Corresponding author. Fax: +886-7-5254099.
E-mail address: jacobc@mail.nsysu.edu.tw (J.C. Huang).

0254-0584/03/$ – see front matter © 2003 Published by Elsevier Science B.V.
doi:10.1016/S0254-0584(03)00168-8

structural materials in transportation vehicles or light-weight enclosures for computer, communication and consumer electronic (3C) products [17–28]. Among numerous literatures and reference books (e.g. [29,30]) on preferred orientation, the textures in cubic materials are predominantly discussed. The systematic presentation for texture components and texture evolutions for hexagonal materials are rarely found. This was mainly because that there have been very limited research reports systematically concentrated on the texture in hexagonal materials. In this review paper, the possible major texture components in hexagonal structural materials with different c/a ratios is simulated by our software and presented in a systematic way, mainly dealing with the deformation texture and recrystallization texture as well as anisotropy of textured hexagonal close packed (HCP) materials.

2. Representation of texture in hexagonal materials

The texture in rolled sheet hexagonal metals, are commonly represented by $\{h\,k\,i\,l\}\langle u\,v\,t\,w\rangle$, which means that the $\{h\,k\,i\,l\}$ planes of these grains lie parallel to the sheet plane, whereas their $\langle u\,v\,t\,w\rangle$ direction point parallel to the rolling direction. When the texture is less complex, it is possible to describe the texture by means of a series of pole figures constructed by simple X-ray diffraction methods. However, the information contained in pole figures is incomplete and at best semi-quantitative. In fact, it is frequently not sufficient to fully determine the true and complete textures if the crystallites possess more than one preferred (ideal) orientation. The more complete orientation distribution function is unfortunately, however, not directly measured by simple X-ray diffraction, and need further derivations and calculations based on a number of experimentally measured pole figures.

2.1. Pole figure

The pole figure is the two-dimensional stereographic projection, with a specified orientation relative to the specimen, which shows the variation of pole density with pole orientation for a selected set of crystal plane $\{h\,k\,i\,l\}$. The most popular way to obtain the incomplete pole figure is the "Schulz reflection method" [31]. With respect to the hexagonal materials, there are slight differences in the standard $\{h\,k\,i\,l\}$ stereographic projections due to the different ratios of lattice constants, c/a. Standard stereographic projections for different c/a ratios can be easily simulated by commercially available programs, such as Diffract [32] or CaRIne Crystallography [33]. In the hexagonal materials, the $\{0\,0\,0\,1\}$ basal texture is frequently present. The ideal pole figures of some important texture components, self simulated in our laboratory for $c/a = 1.633$, are shown in Fig. 1. These are perfectly suitable for Mg base alloys since their c/a ratios are ~1.624. Only very slight modifications are needed for other hexagonal materials with different c/a ratios.

2.2. Orientation distribution function

The information contained in pole figures is incomplete and semi-quantitative at best. One way of removing this difficulty is to use the crystallite orientation distribution function, which essentially describes the frequency of occurrence of particular orientations in a three-dimensional (Euler) orientation space. This space is defined by three angles (Euler angle), which constitute a set of three consecutive rotations that bring the crystallographic axes (e.g. a_1- or c-axis) of each crystallite into coincidence with the specimen axes.

The definition of the three Euler angles is explained below. There have been two systems commonly used in literatures. Fig. 2 shows the definition of the three Euler angles by the Roe system [34]. For example, one begins with an orientation of the crystal coordinate system in which the axes are parallel to those of the sample coordinate system. The crystal coordinate system is then first rotated about the Z'-axis through the angle ψ, then about Y'-axis (in its new orientation) through θ and, finally, once again about the Z'-axis through φ. The rotation g defined in the Roe system is thus represented by the three Euler angles ψ, θ, φ as:

$$g = \{\psi, \theta, \varphi\} \tag{1}$$

It is customary to represent the three parameters of rotation $g\{\psi, \theta, \varphi\}$ as coordinates in a three-dimensional space or Euler space. The Euler space thus forms a three-dimensionally periodic lattice with unit cell $\{2\pi, 2\pi, 2\pi\}$. The asymmetric unit is, however, restricted to the region $\{2\pi, \pi, 2\pi\}$ by a glide plane. In addition to the crystal symmetry in hexagonal materials, the sample can also possess statistic symmetry of the orientation distribution. Then, the Euler space was restricted to the region $\{\pi/2, \pi/2, \pi/3\}$. In other words, one only needs to present the ψ, θ, φ angles for hexagonal ODF up to 90, 90, and 60°. In the same way, the Euler space can also be established by the Bunge system [35] in terms of ϕ_1, ϕ, ϕ_2, which are the angles for different ways of rotation as depicted in Fig. 3.

If one denotes dV the volume elements of the sample which possess the orientation g within the element of orientation dg, and denotes the V the total sample volume, then, an orientation distribution function $f(g)$, is defined by:

$$\frac{\mathrm{d}V}{V} = f(g)\,\mathrm{d}g \tag{2}$$

where $\mathrm{d}g = 1/8\pi^2 \sin\theta\,\mathrm{d}\psi\,\mathrm{d}\theta\,\mathrm{d}\varphi$. The function $f(g)$, which depends on the orientation g, can be developed in a series of generalized spherical harmonics [30]:

$$f(\psi, \theta, \varphi) = \sum_{l=0}^{\infty} \sum_{m=-l}^{+l} \sum_{n=-l}^{+l} W_{lmn} Z_{lmn}(\xi) \times \exp(-\mathrm{i}m\psi)\exp(-\mathrm{i}n\varphi) \tag{3}$$

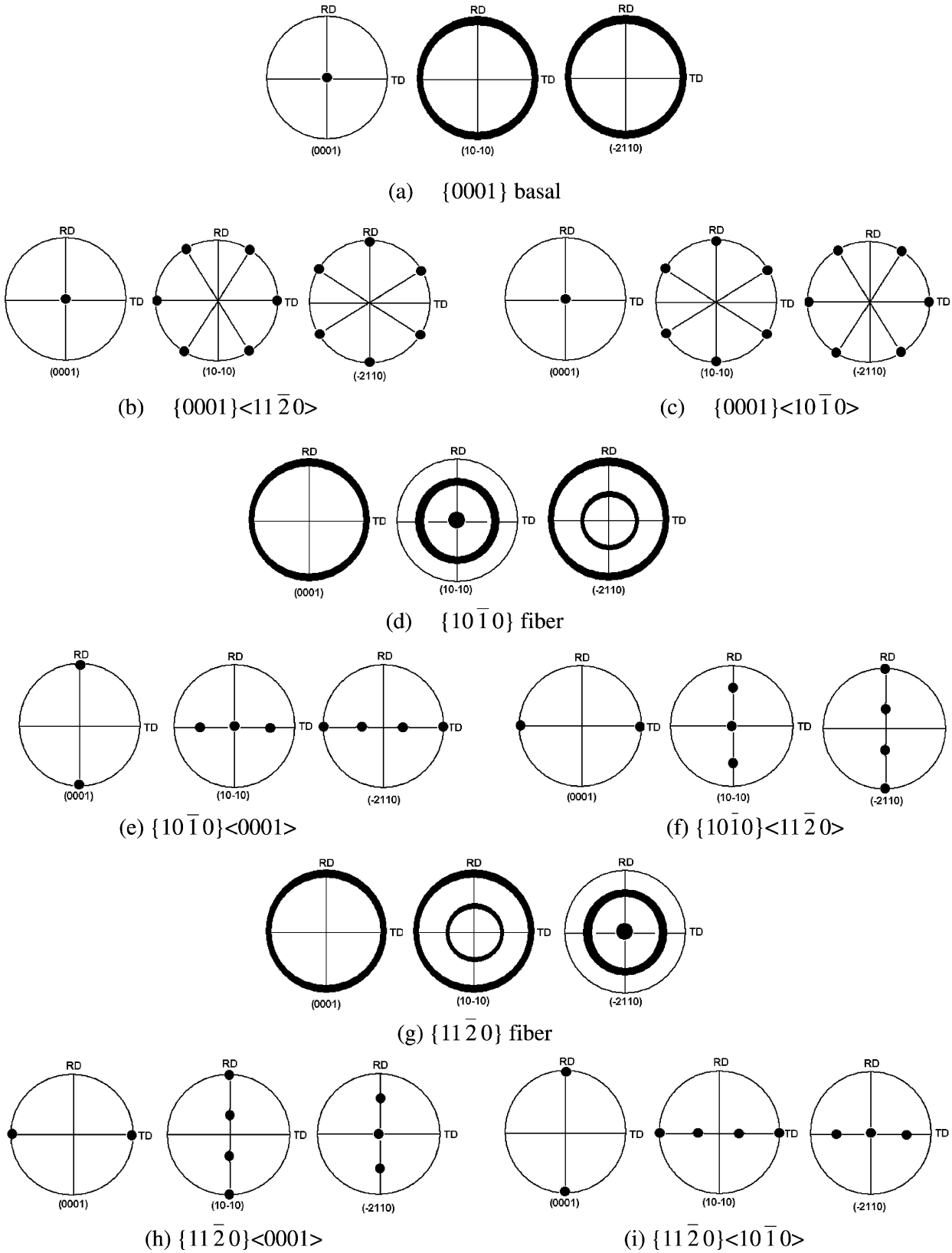

Fig. 1. Ideal pole figures of some important texture components for Mg ($c/a = 1.624$).

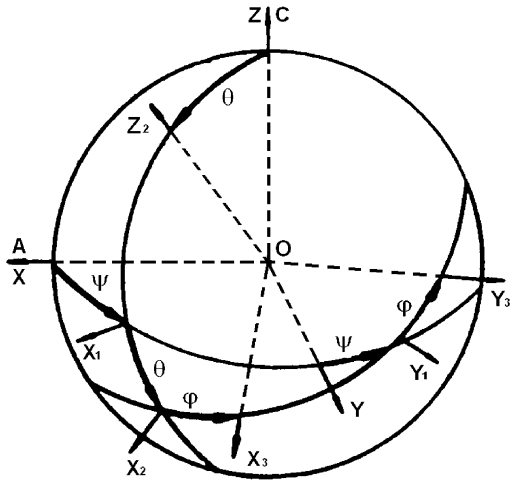

Fig. 2. Illustration of the Euler angles ψ, θ, ϕ in accordance with the Roe system.

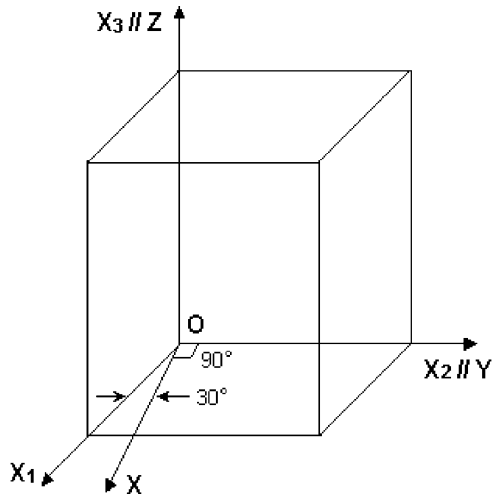

Fig. 4. Schematic diagram illustrating the hexagonal system represented by $\{O X_1 X_2 X_3\}$ and the cubic system represented by $\{O X Y Z\}$.

where W_{lmn} are the coefficients of the series of generalized spherical harmonics; $\xi = \cos\theta$; $Z_{lmn}(\xi)$ are the certain generalizations of the associated Jacob function. Mathematical methods have been developed that allow an ODF to be calculated from numerical data obtained from several experimental pole figures.

The ODF supplies a detailed description of texture components of grains in polycrystalline materials. Each component g is defined by the angles ψ, θ and φ or ϕ_1, ϕ and ϕ_2 that correspond to a rotation about the *Z*–*Y*–*Z*-axes in the Roe system or *Z*–*X*–*Z*-axes in the Bunge system, respectively.

However, the procedures described above cannot be used for the hexagonal crystals. For the hexagonal case, there lacks a direct correlation between ODF and crystallographic planes and directions. To express texture components in a hexagonal system, it is necessary to introduce a change between the hexagonal and cubic systems. In a cubic system, the [1 0 0], [0 1 0] and [0 0 1] directions are parallel to the *X*-, *Y*- and *Z*-reference axes, respectively. In the case of hexagonal systems, the $[1\,0\,\bar{1}\,0]$, $[1\,1\,\bar{2}\,0]$ and [0 0 0 1] directions are parallel to the X_1-, *Y*- and *Z*-reference axes, as shown in Fig. 4. Therefore, we need to find the relationship between the orientation $g\{\psi, \theta, \varphi\}$ (in the Roe system) and $\{h\,k\,i\,l\}\langle u\,v\,t\,w\rangle$, which can be expressed by:

$$\begin{bmatrix} h \\ k \\ i \\ l \end{bmatrix} = \begin{bmatrix} \sqrt{3} & -\frac{1}{2} & 0 \\ 0 & 1 & 0 \\ -\sqrt{3} & -\frac{1}{2} & 0 \\ 0 & 0 & c/a \end{bmatrix} \begin{bmatrix} -\sin\theta\cos\varphi \\ \sin\theta\sin\varphi \\ \cos\theta \end{bmatrix} \tag{4}$$

and

$$\begin{bmatrix} u \\ u \\ t \\ w \end{bmatrix} = \begin{bmatrix} \frac{1}{\sqrt{3}} & -\frac{1}{3} & 0 \\ 0 & \frac{2}{3} & 0 \\ -\frac{1}{\sqrt{3}} & -\frac{1}{3} & 0 \\ 0 & 0 & c/a \end{bmatrix} \times \begin{bmatrix} \cos\psi\cos\theta\cos\varphi - \sin\theta\sin\varphi \\ -\cos\psi\cos\theta\sin\varphi - \sin\psi\cos\varphi \\ \cos\psi\sin\theta \end{bmatrix} \tag{5}$$

Similarly, the relationship between the orientation $g\{\phi_1, \phi, \phi_2\}$ and $\{h\,k\,i\,l\}\langle u\,v\,t\,w\rangle$ in the Bunge system can be expressed by:

$$\begin{bmatrix} h \\ k \\ i \\ l \end{bmatrix} = \begin{bmatrix} \frac{\sqrt{3}}{2} & -\frac{1}{2} & 0 \\ 0 & 1 & 0 \\ -\frac{\sqrt{3}}{2} & -\frac{1}{2} & 0 \\ 0 & 0 & c/a \end{bmatrix} \begin{bmatrix} \sin\phi_2\sin\phi \\ \cos\phi_2\sin\phi \\ \cos\phi \end{bmatrix} \tag{6}$$

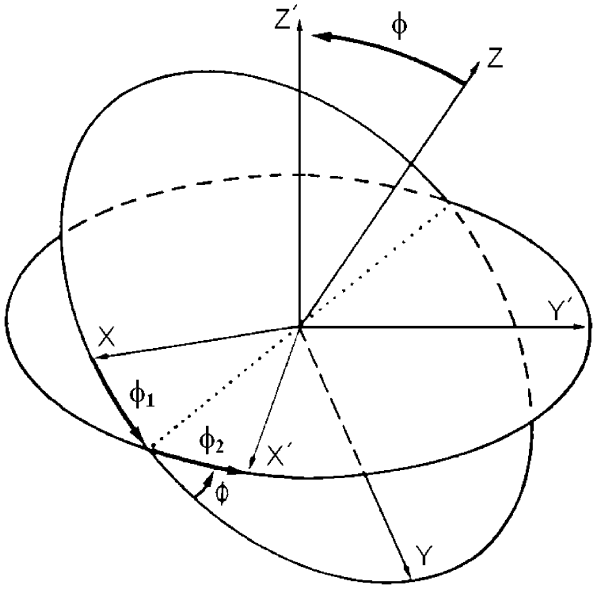

Fig. 3. Illustration of the Euler angles ϕ_1, ϕ, ϕ_2 in accordance with the Bunge system.

Table 1
Texture characteristics in HCP materials (Roe system)

Texture component	Constant φ (°)	θ (°)	ψ (°)
Basal fiber $\{0\,0\,0\,1\}$	0–60	0	0–90
Basal fiber $\{h\,k\,i\,l\}$	$[1\,0\,\bar{1}\,0]\|[h\,k\,i\,0]$[a]	$[0\,0\,0\,1]\|[h\,k\,i\,l]$[a]	0–90
$\{0\,0\,0\,1\}\langle 1\,0\,\bar{1}\,0\rangle$	0/60	0	0.60/0.60
	$\varphi + \psi = 60$	0	$\varphi + \psi = 60$
$\{0\,0\,0\,1\}\langle 1\,1\,\bar{2}\,0\rangle$	30	0	0.30
	$\varphi + \psi = 30$	0	$\varphi + \psi = 30$
Fiber $\{1\,0\,\bar{1}\,0\}$	0/60	90	0–90
$\{1\,0\,\bar{1}\,0\}\langle 0\,0\,0\,1\rangle$	0/60	90	0
$\{1\,0\,\bar{1}\,0\}\langle 1\,1\,\bar{2}\,0\rangle$	0/60	90	90
Fiber $\{1\,1\,\bar{2}\,0\}$	30	90	0–90
$\{1\,1\,\bar{2}\,0\}\langle 0\,0\,0\,1\rangle$	30	90	0
$\{1\,1\,\bar{2}\,0\}\langle 1\,0\,\bar{1}\,0\rangle$	30	90	90

[a] $[1\,0\,\bar{1}\,0]\|[h\,k\,i\,0]$ means the angle in-between $[1\,0\,\bar{1}\,0]$ and $[h\,k\,i\,l]$; the same as $[0\,0\,0\,1]\|[h\,k\,i\,l]$.

Table 2
Texture characteristics in HCP materials (Bunge system)

Texture component	Constant ϕ_2 (°)	ϕ (°)	ϕ_1 (°)
Basal fiber $\{0\,0\,0\,1\}$	0–60	0	0–90
Basal fiber $\{h\,k\,i\,l\}$	$[2\,\bar{1}\,\bar{1}\,0]\|[h\,k\,i\,0]$	$[0\,0\,0\,1]\|[h\,k\,i\,l]$	0–90
$\{0\,0\,0\,1\}\langle 1\,0\,\bar{1}\,0\rangle$	0/60	0	0.60/0.60
	$\phi_2 + \phi_1 = 60$	0	$\phi_2 + \phi_1 = 60$
$\{0\,0\,0\,1\}\langle 1\,1\,\bar{2}\,0\rangle$	0/30	0	0.90/0.60
	$\phi_2 + \phi_1 = 30$	0	$\phi_2 + \phi_1 = 30$
Fiber $\{1\,0\,\bar{1}\,0\}$	30	90	0–90
$\{1\,0\,\bar{1}\,0\}\langle 0\,0\,0\,1\rangle$	30	90	90
$\{1\,0\,\bar{1}\,0\}\langle 1\,1\,\bar{2}\,0\rangle$	30	90	0
Fiber $\{1\,1\,\bar{2}\,0\}$	0/60	90	0–90
$\{1\,1\,\bar{2}\,0\}\langle 0\,0\,0\,1\rangle$	0/60	90	90
$\{1\,1\,\bar{2}\,0\}\langle 1\,0\,\bar{1}\,0\rangle$	0/60	90	0

and

$$\begin{bmatrix} u \\ v \\ t \\ w \end{bmatrix} = \begin{bmatrix} \frac{2}{3} & -\frac{1}{3} & 0 \\ 0 & \frac{2}{3} & 0 \\ -\frac{2}{3} & -\frac{1}{3} & 0 \\ 0 & 0 & c/a \end{bmatrix} \times \begin{bmatrix} \cos\phi_1\cos\phi_2 - \sin\phi_1\sin\phi_2\cos\phi \\ -\cos\phi_1\sin\phi_2 - \sin\phi_1\cos\phi_2\cos\phi \\ \sin\phi_1\sin\phi \end{bmatrix} \quad (7)$$

Here, the $\{h\,k\,i\,l\}$ planes of these grains in hexagonal materials lie parallel to the plane of the sheet, whereas their $\langle u\,v\,t\,w\rangle$ directions point parallel to the rolling direction. It is noted that, owing to the symmetry of unit cell and textures of hexagonal materials, the orientation space (or the Euler space), however, is restricted to a smaller region $\{\pi/2, \pi/2, \pi/3\}$. This restriction is also valid for all texture components in hexagonal materials. Furthermore, the effect of c/a ratio on the Miller indices of $\{h\,k\,i\,l\}$ planes and $\langle u\,v\,t\,w\rangle$ directions will impose restriction to the indices of l and w (i.e. $l = (c/a)\cos\theta$ and $w = (c/a)\cos\psi\sin\theta$). The characteristics of some important texture components for the constant φ or ϕ_2 sections of ODF in hexagonal materials with an ideal c/a ratio are listed in Tables 1 and 2 for the Roe and Bunge systems, respectively.

Based on the data in Tables 1 and 2, the ideal ODF distribution positions for selected important texture components or low index orientations for selected sections of fixed ϕ_2 angles are systematically simulated in our laboratory and are shown in Fig. 5.

3. Texture components in hexagonal materials

Textures in the hexagonal metals have attracted significant interest. From a deformation mechanistic point of view, HCP metals are quite different from cubic metals in that limited slip systems are available and twinning frequently provides significant, if not dominant, deformation modes. In what follows, the typical texture components observed in various hexagonal materials are reviewed and compared.

3.1. Fiber texture

Fig. 6 shows the inverse pole figures for a high purity Ti that has been deformed in two different ways [30]. The first

example in Fig. 6a shows the texture in materials that had been uniaxially extruded to a von Mises' equivalent strain of 1.75. A fiber texture is present with a maximum at the $\langle 1\,0\,\bar{1}\,0\rangle$ position, in a way such that all the basal plane normals $\langle 0\,0\,0\,1\rangle$ are perpendicular to the extrusion axis. This is termed as the "cylindrical texture", commonly observed in extruded rods of hexagonal materials. The second example in Fig. 6b is the same material that has been upset and then cross-rolled to a von Mises' equivalent strain of 1.98. This process gave rise to a fiber texture for the plate normal that is about 25° away from $\langle 0\,0\,0\,1\rangle$ which is approximately equivalent to the position in-between $\langle 1\,1\,\bar{2}\,4\rangle$ and $\langle 1\,0\,\bar{1}\,3\rangle$.

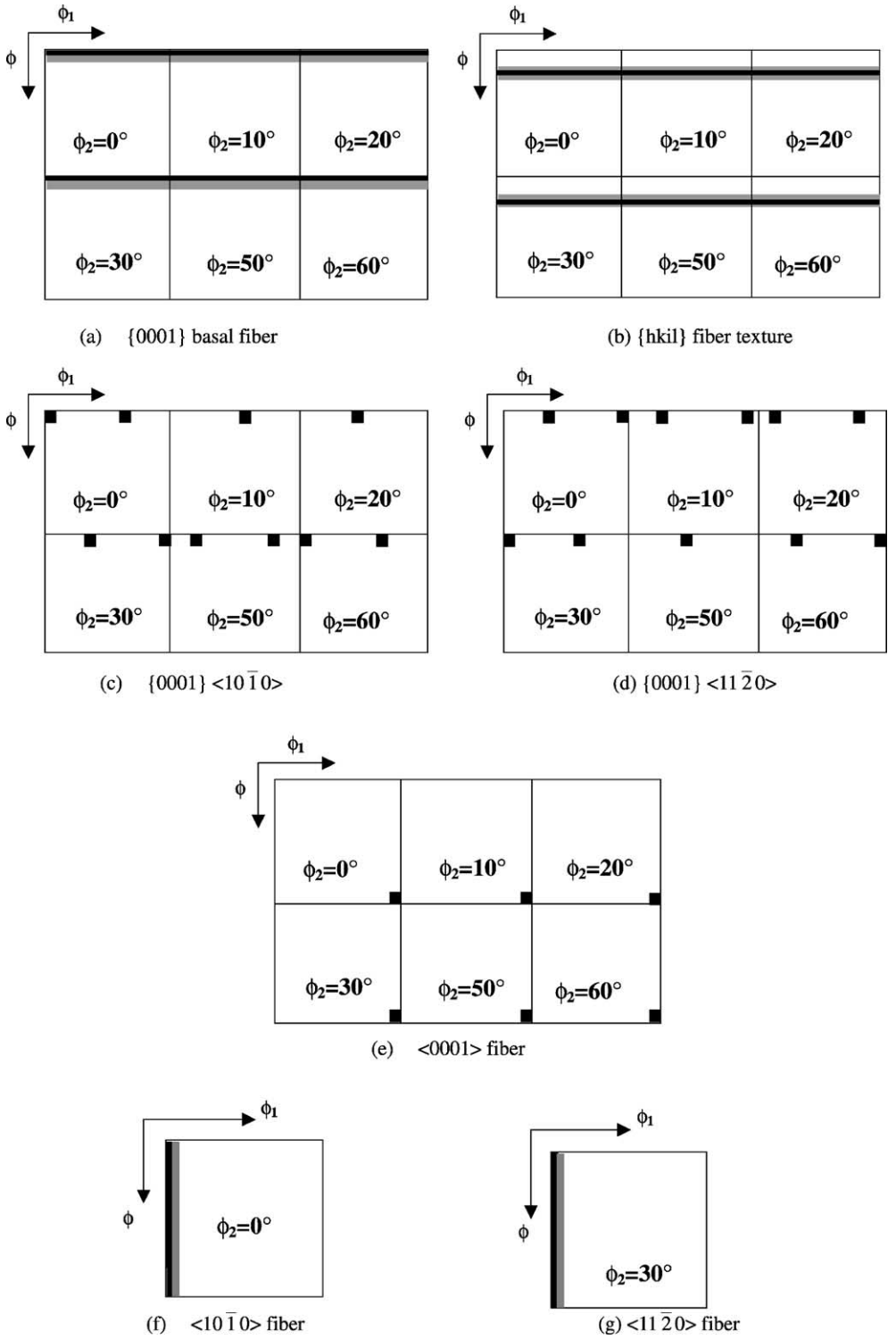

Fig. 5. The ideal ODF positions for some low index orientation of the HCP crystalline structure.

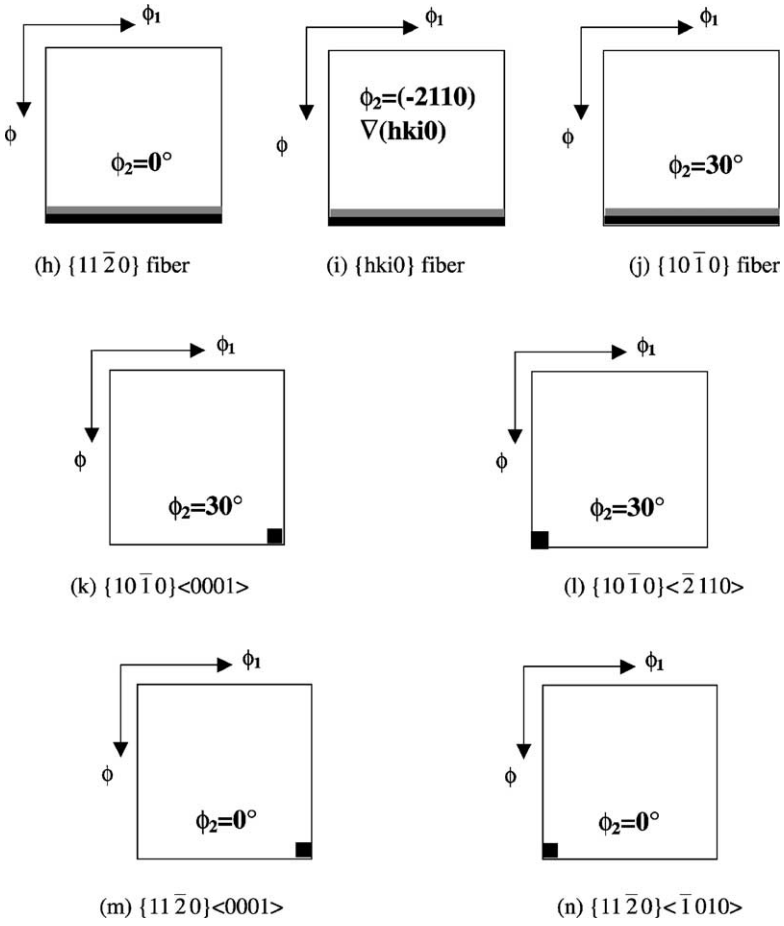

Fig. 5. (*Continued*).

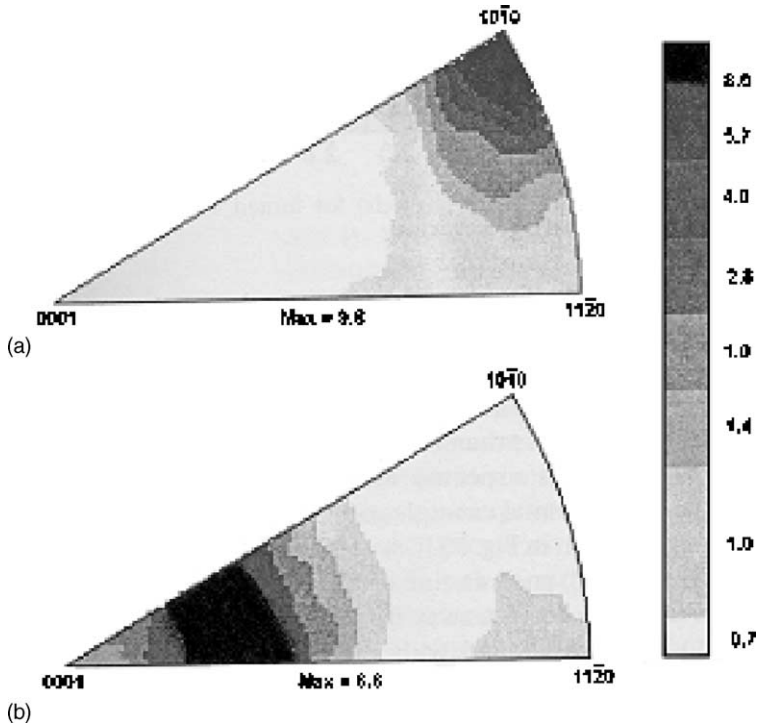

Fig. 6. Inverse pole figures for high purity Ti: (a) extruded to a strain of 1.75 (for extrusion axis); and (b) forged and cross-rolled to a strain of 1.98 (for plate normal) [30].

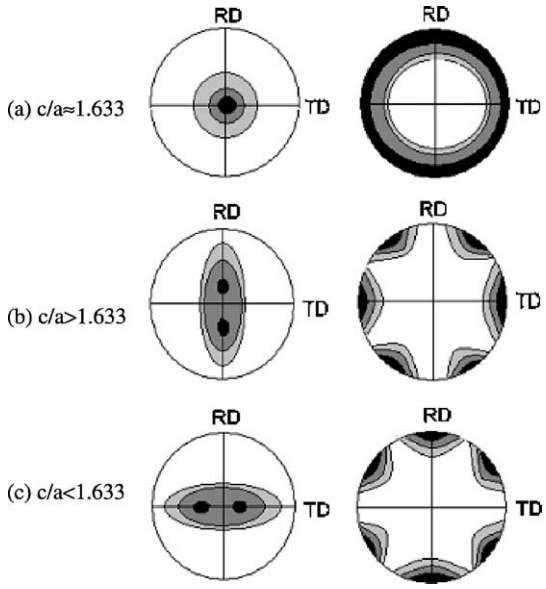

Fig. 7. Simulated rolling texture in HCP metals with *c*/*a* ratio: (a) approximately equal to 1.633; (b) >1.633; and (c) <1.633.

3.2. Rolling texture

The textures of cold-rolled hexagonal metals and alloys can be categorized into three groups according to their *c*/*a* ratios, namely materials with *c*/*a* ratios greater than, approximately equal to, and less than the ideal value of 1.633. The simulated (0 0 0 2) and (1 0 $\bar{1}$ 0) pole figures by our software for the cold-rolled sheet textures with different *c*/*a* categories are schematically illustrated in Fig. 7. Experimental results of the (0 0 0 2) and (1 0 $\bar{1}$ 0) pole figures for rolled Mg (*c*/*a* = 1.624), Zn (1.856) and Ti (1.588) [8], shown in Fig. 8, are in good agreement with the predictions.

Metals and alloys with *c*/*a* ratios approximately equal to the ideal *c*/*a* ratio of 1.633, such as Mg, tend to form basal fiber textures (as in Figs. 7a and 8a) during rolling. The origin of such textures may be understood in terms of the slip systems operating on basal planes. Metals and alloys with *c*/*a* ratios above the ideal, such as Zn (1.856) and Cd (1.885), tend to exhibit textures with basal poles tilted ±15–25° away from the normal direction toward the rolling direction, the ⟨1 1 $\bar{2}$ 0⟩ poles aligned with the rolling direction, and the ⟨1 0 $\bar{1}$ 0⟩ directions pointed parallel to the transverse direction (Figs. 7b or 8b). Such textures are due to the combination of basal slip and large-scale twinning. It should be noted that twining in HCP materials can be classified into two groups based on the critical *c*/*a* ratio of $\sqrt{3}$ (= 1.732) [36], below or above this value the twin will form upon compression or tension, respectively. Both Zn and Cd will fall in the same group as their *c*/*a* ratios are both above 1.732. In this paper, the influence from slip system operation is more emphasized, while the factor played by twinning is less addressed. Finally, the metals and alloys, possessing *c*/*a* ratio less than 1.633 such as Zr (1.589) and Ti (1.587), tend to form textures with basal poles tilted ±20–40° away from the normal direction toward the transverse direction, the ⟨1 0 $\bar{1}$ 0⟩ poles aligned with the rolling direction, and the ⟨1 1 $\bar{2}$ 0⟩ directions pointed parallel to the transverse direction (Figs. 7c or 8c). In the latter case, slip on prismatic planes is largely responsible for textures of these types with basal pole spreading. In general, the *c*/*a* ratio reflects the activation of the different slip systems.

Tables 3 and 4 list the commonly observed slip systems in many HCP metals and two DO_{19} crystalline materials.

Table 3
Typical slip systems observed in some HCP metals

Element	*c*/*a*	Deviation (%) from the ideal *c*/*a* = 1.633	Principal slip system	Secondary slip system	Other slip system
Cd	1.886	+15.5	Basal {0 0 0 1}⟨1 1 $\bar{2}$ 0⟩	Pyramidal {1 1 $\bar{2}$ 2}⟨1 1 $\bar{2}$ 3⟩	Prismatic {1 0 $\bar{1}$ 0}⟨1 1 $\bar{2}$ 0⟩ Pyramidal {1 0 $\bar{1}$ 1}⟨1 1 $\bar{2}$ 0⟩
Zn	1.856	+13.6	Basal {0 0 0 1}⟨1 1 $\bar{2}$ 0⟩	Pyramidal {1 1 $\bar{2}$ 2}⟨1 1 $\bar{2}$ 3⟩	Prismatic {1 0 $\bar{1}$ 0}⟨1 1 $\bar{2}$ 0⟩
Mg	1.624	−0.6	Basal {0 0 0 1}⟨1 1 $\bar{2}$ 0⟩	Prismatic {1 0 $\bar{1}$ 0}⟨1 1 $\bar{2}$ 0⟩	Pyramidal {1 0 $\bar{1}$ 1}⟨1 1 $\bar{2}$ 0⟩{1 1 $\bar{2}$ 2}⟨1 1 $\bar{2}$ 3⟩
Co	1.623	−0.6	Basal {0 0 0 1}⟨1 1 $\bar{2}$ 0⟩	None	None
Zr	1.593	−2.4	Prismatic {1 0 $\bar{1}$ 0}⟨1 1 $\bar{2}$ 0⟩	Basal {0 0 0 1}⟨1 1 $\bar{2}$ 0⟩	Pyramidal {1 0 $\bar{1}$ 1}⟨1 1 $\bar{2}$ 0⟩{1 1 $\bar{2}$ 2}⟨1 1 $\bar{2}$ 3⟩
Ti	1.588	−2.8	Prismatic {1 0 $\bar{1}$ 0}⟨1 1 $\bar{2}$ 0⟩	Basal {0 0 0 1}⟨1 1 $\bar{1}$ 0⟩	Pyramidal {1 0 $\bar{1}$ 1}⟨1 1 $\bar{2}$ 0⟩{1 1 $\bar{2}$ 2}⟨1 1 $\bar{2}$ 3⟩
Hf	1.581	−3.2	Prismatic {1 0 $\bar{1}$ 0}⟨1 1 $\bar{2}$ 0⟩	Basal {0 0 0 1}⟨1 1 $\bar{2}$ 0⟩	
Be	1.568	−4.0	Basal {0 0 0 1}⟨1 1 $\bar{2}$ 0⟩	Prismatic {1 0 $\bar{1}$ 0}⟨1 1 $\bar{1}$ 0⟩	Pyramidal {1 0 $\bar{1}$ 1}⟨1 1 $\bar{2}$ 0⟩{1 1 $\bar{2}$ 2}⟨1 1 $\bar{2}$ 3⟩

Table 4
Typical slip systems observed in two DO_{19} alloys

Alloy	*c*/*a*	Deviation (%) from the ideal *c*/*a* = 0.816	Principal slip system	Secondary slip system	Other slip system
Ti_3Al	0.804	−1.57	Prismatic {1 0 $\bar{1}$ 0}⟨1 1 $\bar{2}$ 0⟩	Basal {0 0 0 1}⟨1 1 $\bar{2}$ 0⟩	Pyramidal {1 0 $\bar{1}$ 1}⟨1 1 $\bar{2}$ 0⟩{1 1 $\bar{2}$ 2}⟨1 1 $\bar{2}$ 3⟩
Mn_3Sn	0.800	−2.08	Basal {0 0 0 1}⟨1 1 $\bar{2}$ 0⟩	Prismatic {1 0 $\bar{1}$ 0}⟨1 1 $\bar{2}$ 0⟩	Pyramidal {1 0 $\bar{1}$ 1}⟨1 1 $\bar{2}$ 0⟩

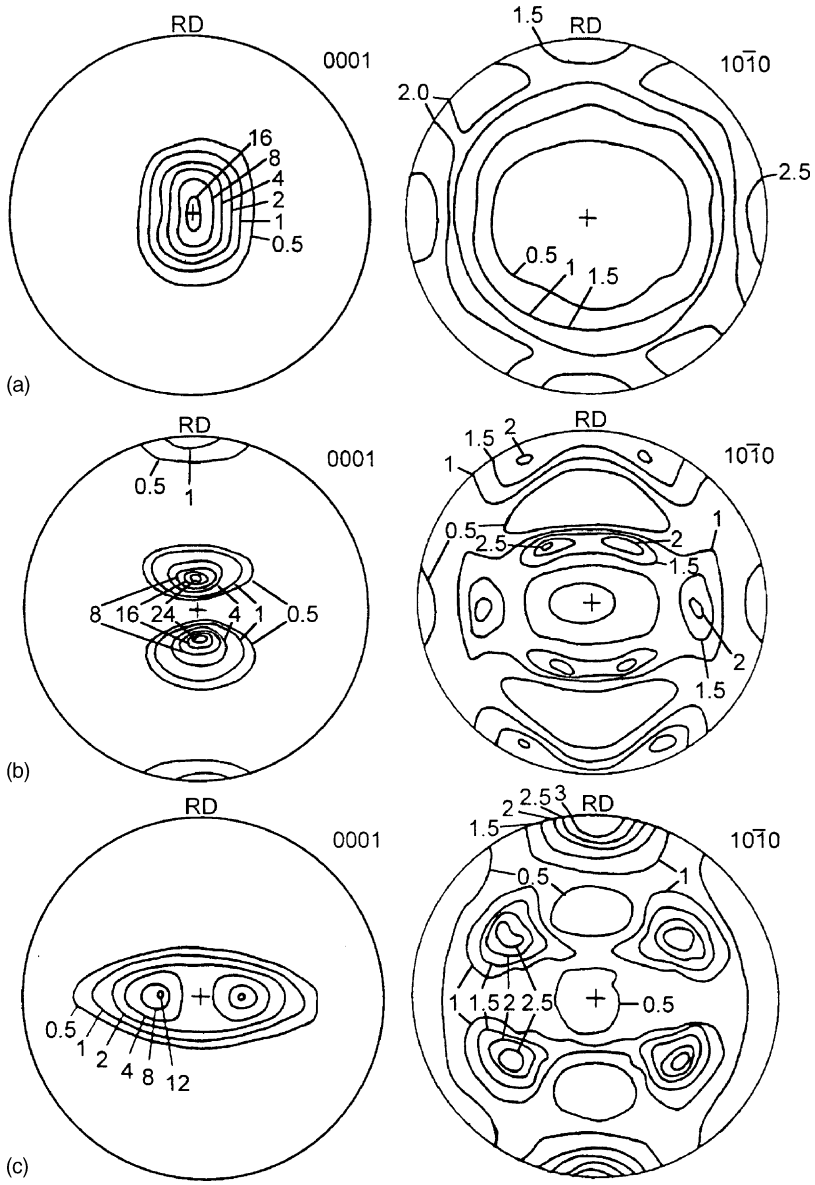

Fig. 8. Experimental (0 0 0 2) and (1 0 $\bar{1}$ 0) pole figures for (a) Mg, (b) Zn, and (c) Ti, showing the ⟨0 0 0 1⟩ fiber texture for Mg, RD split for Zn, and TD split for Ti [30].

The main character of HCP deformation texture can be traced on the base of Tables 3 and 4. As a rough guild line, the basal $\{0\,0\,0\,1\}\langle 1\,1\,\bar{2}\,0\rangle$ slip will result in the basal texture for Mg ($c/a = 1.624$). The combination of basal $\{0\,0\,0\,1\}\langle 1\,1\,\bar{2}\,0\rangle$ slip and pyramidal $\{1\,1\,\bar{2}\,\bar{2}\}\langle 1\,1\,\bar{2}\,3\rangle$ slip in Zn (1.856) will result in the textures with basal poles tilted away from the normal direction toward the rolling direction. And the combination of prismatic $\{1\,0\,\bar{1}\,0\}\langle 1\,1\,\bar{2}\,0\rangle$ slip and basal $\{0\,0\,0\,1\}\langle 1\,1\,\bar{2}\,0\rangle$ slip in Ti (1.587) and Zr (1.589) will result in the textures with basal poles tilted away from the normal direction toward the transverse direction.

When compared to crystal systems like face-centered cubic (FCC) or body-centered cubic (BCC), the HCP metals exhibit a wider variety of deformation textures. Historically, HCP metals have been categorized in terms of c/a ratio, and the observed rolling textures are also similarly categorized. The distinct textures are actually due to the combined effects of c/a ratio and the fact that different HCP metals deform by different slip and/or twinning modes.

The qualitative observation of a "Ti- or Zr-type rolling texture" after hot strip extrusion of a Mg 14.8 at.% Li alloy at 425 °C was proposed as the evidence for increased prismatic slip in the Mg–Li alloys [20], since the primary deformation mode in Ti and Zr is the prismatic ⟨a⟩ slip. However, when the same alloy was cold-rolled after extrusion, the texture tended to move back towards the typical "Mg-type texture". We believe that the prismatic ⟨a⟩ slip in the Mg base alloys is actually a thermally activated deformation mode, and its role during high temperature deformation of Mg–Li alloys may be substantial.

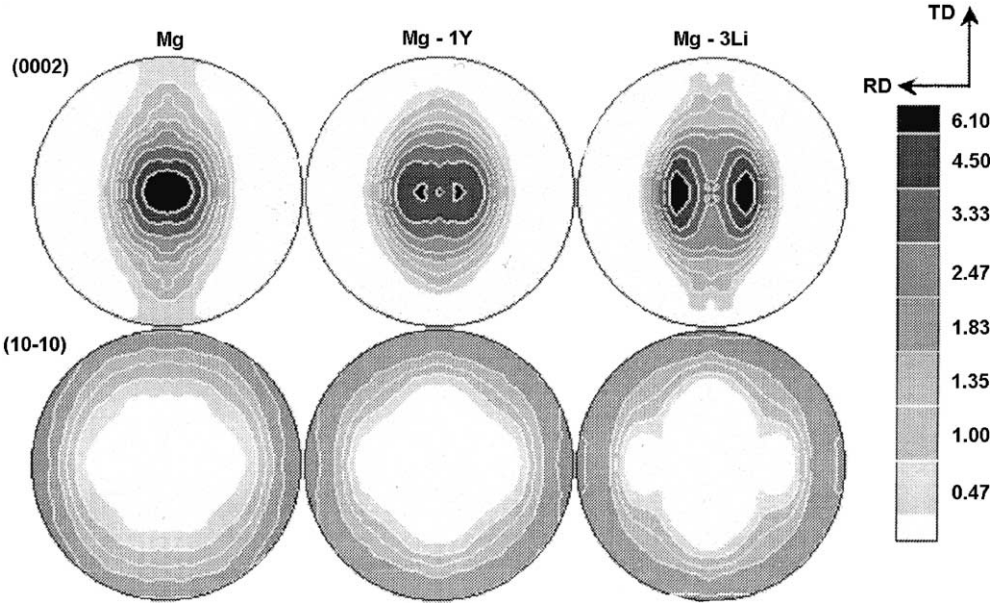

Fig. 9. Experimental (0 0 0 2) and (1 0 $\bar{1}$ 0) pole figures for plane strain compression texture ($\varepsilon = 30\%$) in pure Mg, Mg 1 wt.% Y, and Mg 3 wt.% Li alloys [20].

The influence of alloying elements of Ti and Y in magnesium base alloys on their compression textures was investigated [20]. Based on the experimental results (Fig. 9) and texture simulations, the polycrystalline plasticity modeling approach was used to simulate the observed textures by varying the critical resolved shear stress (CRSS) values for possible deformation modes (Table 5). Guidance in selecting the CRSS values for each deformation mode was obtained from data generated from single crystal studies. The simulated results appear to be similar to the experimental measurements when the relative CRSS values are selected so that the ratios of basal $\langle a \rangle$:prismatic $\langle a \rangle$:pyramidal $\langle c+a \rangle$:tension twin are 1:3:4:2, as seen in Fig. 10. The simulated results and experimental evidence demonstrate that at room temperature and below, the enhancement of the pyramidal $\langle c+a \rangle$ slip mode may be more important than any possible enhancement of prismatic $\langle a \rangle$ slip.

In short summary, the deformation model in hexagonal crystals is based on the following three distinct slip systems and one twinning system: (i) basal $\{0\,0\,0\,1\}\langle 1\,1\,\bar{2}\,0\rangle$; (ii) prismatic $\{1\,0\,\bar{1}\,0\}\langle 1\,1\,\bar{2}\,0\rangle$; (iii) pyramidal $\{1\,1\,\bar{2}\,2\}\langle 1\,1\,\bar{2}\,\bar{3}\rangle$ and $\{1\,0\,\bar{1}\,1\}\langle 1\,1\,\bar{2}\,0\rangle$; as well as (iv) twinning $\langle 1\,0\,\bar{1}\,0\rangle$ slip on $\{1\,0\,\bar{1}\,2\}$. The formation of deformation texture in HCP metals and its alloys will develop in accordance with the relative contributions from the above four deformation paths. Through these deformation processes, the slip plane will gradually rotate toward the rolling plane and the slip direction toward the rolling direction.

Table 5
Deformation modes considered in texture simulations by Suzuki et al. [25]

Mode	Plane	Direction	Relative CRSS[a]
Basal $\langle a \rangle$	$\{0\,0\,0\,2\}$	$\langle 1\,1\,\bar{2}\,0\rangle$	1
Prismatic $\langle a \rangle$	$\{1\,0\,\bar{1}\,0\}$	$\langle 1\,1\,\bar{2}\,0\rangle$	1–12
Pyramidal $\langle c+a \rangle$	$\{1\,1\,\bar{2}\,2\}$	$\langle 1\,1\,\bar{2}\,3\rangle$	1–12
Tensile twin	$\{1\,0\,\bar{1}\,2\}$	$\langle 1\,0\,\bar{2}\,1\rangle$	1–4

[a] The strengths of the different deformation modes were normalized to $\mathrm{CRSS}_{\mathrm{basal}\,\langle a \rangle} = 1$.

3.3. Recrystallization texture

Recrystallization shares several common characteristics as phase transformation in that the replacement of deformed

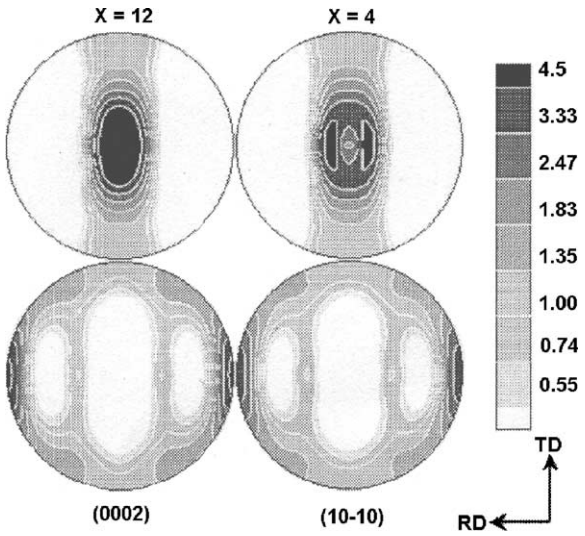

Fig. 10. Simulated (0 0 0 2) and (1 0 $\bar{1}$ 0) pole figures for plane compression textures, using relative CRSS values of 1:3:X:2 for basal:prismatic:$\langle c+a \rangle$:tension twin. Shown in figures are the examples using $X = 12$ and 4 [20].

materials by the nucleation and growth of recrystallized grains, both can lead to drastic changes in texture. The principal differences are (i) the "nuclei" during recrystallization are regions that already exist in the deformed microstructure; and (ii) recrystallization dose not lead to precise orientation relationship between the deformed and recrystallized materials in contrast to the case of phase transformation. Although there might be some approximate orientation relationships present in-between the recrystallized and parent grains, there have been no report in making quantitative predictions for recrystallization texture based on such approximate orientation relationships. It should also be noted that recrystallization does not always lead to changes in texture, particularly when a large volume fraction of second-phase particles are present.

In contrast to the well-established case for the FCC and BCC materials, the recrystallization texture in hexagonal material have been rarely studied. It is not difficult to find texture examples in cubic systems for any combination of alloy and processing modes. Despite the progress made in developing models for recrystallization texture development in cubic systems, such as the oriented nucleation mode, oriented growth mode, or a combination of both [37], however, the texture evolution is still highly sensitive to almost the entire spectrum of metallurgical variables and sometimes difficult to fully predict even for cubic materials.

It is sometimes observed that recrystallization texture components bear crystallographic relationships to the original deformation textures, which may be described by rotations about simple crystal directions. For example, the BCC metals often show ∼25° rotations around ⟨1 1 0⟩ directions and FCC metals 30–40° rotations around ⟨1 1 1⟩ [29]. For HCP metals, rotations of ∼30° around ⟨0 0 0 1⟩ and ∼90° around ⟨1 0 $\bar{1}$ 0⟩ have been reported [37–39]. The basal pole figures of recrystallized HCP metals are often essentially similar to those of rolling textures. The main basal texture components can be explained by the ∼30° rotation about ⟨0 0 0 1⟩ makes orientation change between rolled and annealed textures. In fact, closer examination frequently reveals other types of textural change upon annealing.

The evolution of texture in a low-alloyed titanium T40 sheet, initially deformed by 80% cold rolling, was investigated at different stages of recrystallization process [11]. Fig. 11 shows the ODF of the T40 cold-rolled down to 80%. It can be seen from Fig. 11a that the main peak is centered at a position with $\phi_1 = 0°$, $\phi = 45°$, $\phi_2 = 0°$, i.e. close to (1 1 $\bar{2}$ 3)[1 0 $\bar{1}$ 0], with a very large spread around it, and that a weak secondary peak around the position with $\phi_1 = 0°$, $\phi = 32°$, $\phi_2 = 30°$, i.e. close to (1 0 $\bar{1}$ 3)[1 1 $\bar{2}$ 0], is also present. Fig. 12 shows the section at $\phi_1 = 0°$ for the same T40 sample that has been further annealed at 500 °C for different times [11]. It can be clearly seen that the change in ODF is fairly limited. The orientations with low ϕ angles (i.e. with the *Z*-axis nearly parallel to the normal direction ND) as well as the orientations with high ϕ angles (i.e. with *Z*-axis nearly perpendicular to ND) decrease whereas more orientations appear around positions with $\phi_1 = 0°$, $\phi = 45°$, $\phi_2 = 0°$ and $\phi_1 = 0°$, $\phi = 32°$, $\phi_2 = 30°$, which correspond to the main peak (1 1$\bar{2}$ 3)[1 0 $\bar{1}$ 0] and the weak peak (1 0 $\bar{1}$ 3)[1 1 $\bar{2}$ 0] texture, respectively. This kind of change of texture during primary recrystallization process is called the continuous recrystallization or recrystallization in situ, and often occurs in highly deformed metals [38]. Such continuous recrystallization is mainly contributed by the formation of subgrains via dislocation rearrangement and the growth and coarsening of cells and subgrains. The occurrence of continuous recrystallization or extended recovery is consistent with the high level of stacking fault energy in titanium. It is well established that the extent of recovery is higher in metals or alloys with high stacking fault energy [11]. Fig. 13 shows the constant ϕ_1 sections of a fully recrystallized T40 sample heat treated for 1 h at 700 °C [11]. In this case, secondary recrystallization has taken place. The texture is characterized by a high density in ODF around a position with $\phi_1 = 0°$, $\phi = 32°$, $\phi_2 = 30°$, i.e. close to (1 0 $\bar{1}$ 3)[1 1 $\bar{2}$ 0]. In addition, the "deformation texture component" is shifted around a point at $\phi_1 = 0°$, $\phi = 30°$, $\phi_2 = 0°$, i.e. close to (1 1 $\bar{2}$ 5)[1 0 $\bar{1}$ 0], and remains at a fairly high level. These textural characteristics are then due to a selective grain growth which is influenced by the inheritance of the texture and microstructure developed during the first stage.

As another typical ODF example of recent research on recrystallization texture in ($\alpha_2 + \beta$) Ti_3Al [12], the texture evolution during recrystallization from hot rolling texture in the near-α_2 phase field is presented in Fig. 14. In the $\phi_2 = 0$ and 30° sections of the rolled specimen in Fig. 14a, the orientations are found to be grouped near the (0 0 0 1)//normal direction, indicating that some kind of fiber texture component

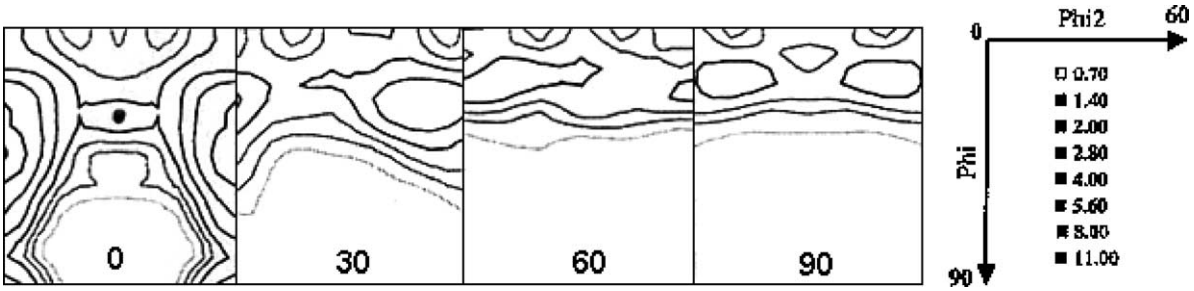

Fig. 11. ODF sections at constant Phi 1 (ϕ_1) for the T40 titanium plate cold-rolled to 80% [11].

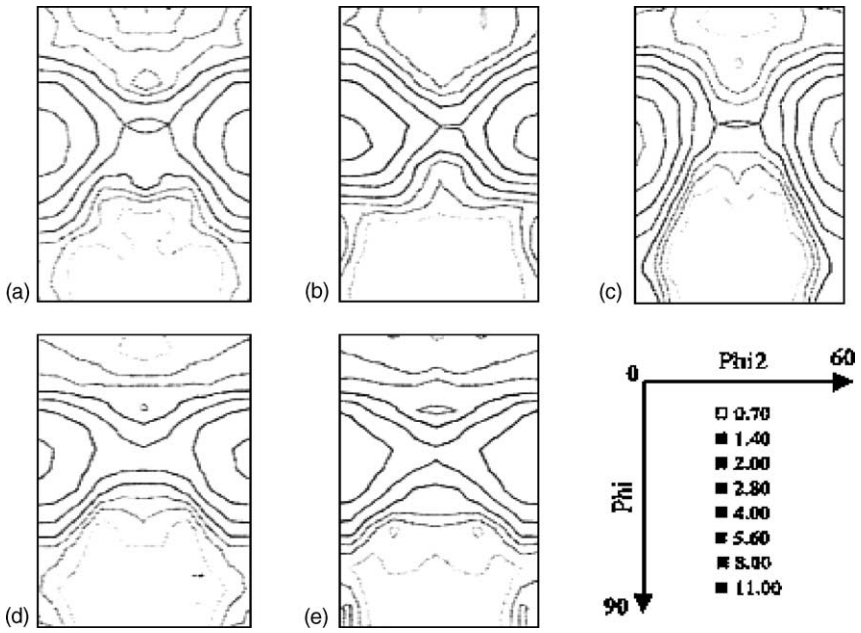

Fig. 12. ODF sections ($\phi_1 = 0°$) for the T40 titanium plate cold-rolled to 80%, followed by annealing at 500 °C: (a) 40 min; (b) 80 min; (c) 160 min; (d) 210 min; and (e) 360 min [11].

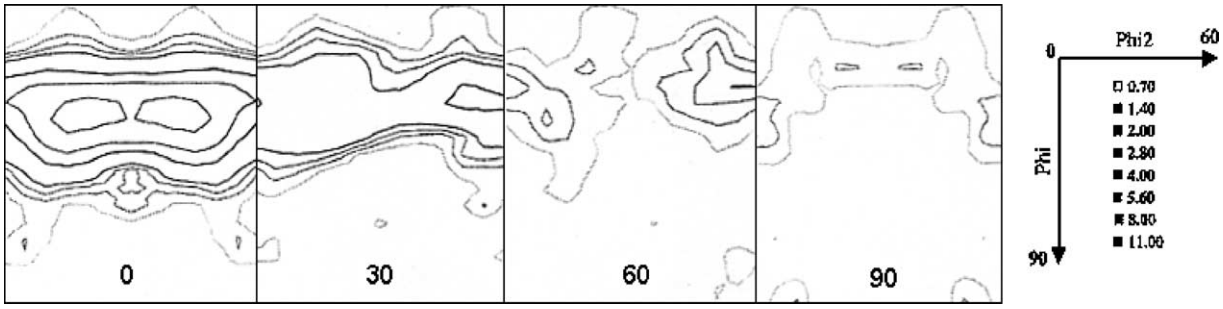

Fig. 13. ODF sections at constant Phi 1 (ϕ_1) for the T40 titanium plate cold-rolled to 80%, followed by full recrystallization at 700 °C for 1 h [11].

is present along that direction. The intensity maximum, however, is shifted away from this exact location. The $\phi_2 = 0°$ section of ODF for the hot rolled material shows that the most intense peaks are present at $\phi_2 \approx 8°$ away from the ideal $(0\,0\,0\,1)(1\,0\,\bar{1}\,0)$ locations. In the $\phi_2 = 30°$ section of ODF, the obvious $\{1\,0\,\bar{1}\,6\}$ fiber has already formed and $(\bar{4}\,\bar{1}\,5\,1)$ and $(\bar{4}\,4\,0\,3)$ directions are oriented. So, It is rationally suspected that the combined deformation mode of basal $\langle a \rangle$ slip and prismatic $\langle a \rangle$ slip of the α_2 phase may have occurred at high temperatures. The $\phi_2 = 0$ and 30° sections of the Ti_3Al material annealed at 900 °C for 1 h in Fig. 14b show the retention of the near basal texture, the fiber being

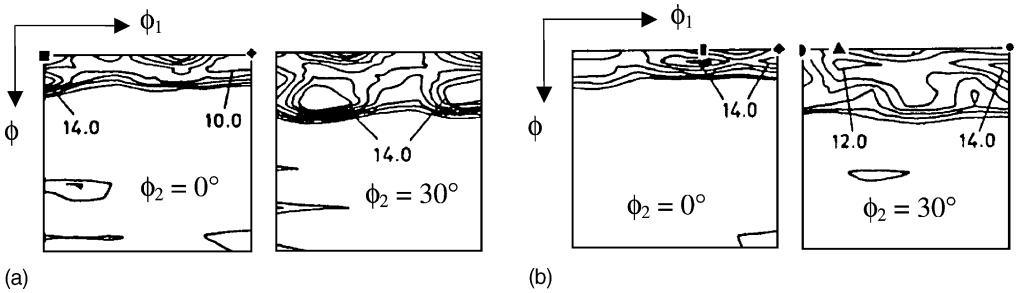

Fig. 14. ODF sections at $\phi_2 = 0$ and 30° for the $(\alpha_2 + \beta)$ Ti_3Al: (a) hot rolled at 900 °C; and (b) after further annealing at 900 °C for 1 h [12].

Table 6
Representative deformation or recrystallization textures commonly observed in hexagonal metals and alloys

Material	Processing	Major texture component	Reference
Cd and Zn	Columnar solidification	$\langle 0\,1\,\bar{1}\,0\rangle$ fiber texture	[39]
Mg	Columnar solidification	$\langle 1\,1\,\bar{2}\,0\rangle$ fiber texture	[39]
HCP metals and alloys	Wire and rod manufacture	$\langle 0\,1\,\bar{1}\,0\rangle$ fiber texture	[39]
Metals with $c/a > 1.623$ (Zn, Cd)	Cold rolling	$\sim\{1\,1\,\bar{2}\,3\}\langle 1\,1\,\bar{2}\,3\rangle$	[30]
Metals with $c/a \approx 1.623$ (Mg, Co)	Cold rolling	$\{0\,0\,0\,1\}\langle 1\,0\,\bar{1}\,0\rangle$	[30]
Metals with $c/a < 1.623$ (Ti, Zr)	Cold rolling	$\sim\{1\,1\,\bar{2}\,2\}\langle 1\,0\,\bar{1}\,0\rangle$	[30]
$(\alpha_2 + \beta)$ Ti_3Al	Hot rolling in near-α_2 phase field (~1123 K)	Mainly $\{0\,0\,0\,1\}\langle 1\,0\,\bar{1}\,0\rangle$, with weak $\{1\,\bar{1}\,0\,6\}$ $[\bar{4}\,\bar{1}\,5\,1]$ and $[\bar{4}\,4\,0\,3]$	[12]
AZ31 Mg alloy	Hot extrusion plate (~570 K)	Mainly $\{0\,0\,0\,1\}$ basal fiber; with weak $\{1\,0\,\bar{1}\,0\}$ and $\{1\,1\,\bar{2}\,0\}$ fibers	[24]
AZ31 Mg alloy	Recrystallization (~723 K) followed by hot extrusion	$\{0\,0\,0\,1\}$ basal and $\{1\,0\,\bar{1}\,0\}$ fibers are retained, $\{1\,1\,\bar{2}\,0\}$ fiber is strengthened	[24]
AZ31 Mg alloy	Secondary recrystallization (~800 K) followed by hot extrusion	$\{1\,1\,\bar{2}\,0\}\langle 1\,0\,\bar{1}\,0\rangle$	[24]
Ti–6Al–4V (α phase)	Hot rolling in α field (~1323 K)	$\{1\,0\,\bar{1}\,0\}\langle 1\,1\,\bar{2}\,0\rangle$	[10]
Ti40	Cold rolling	Strong $\{1\,1\,\bar{2}\,3\}\langle 1\,0\,\bar{1}\,0\rangle$ and weak $\{1\,0\,\bar{1}\,3\}\langle 1\,1\,\bar{2}\,0\rangle$	[11]
Ti40	Fully recrystallization (~973 K for 1 h)	$\{1\,0\,\bar{1}\,3\}\langle 1\,1\,\bar{2}\,0\rangle$	[11]

located at ~8° towards ϕ from the perfect $(0\,0\,0\,1)(u\,v\,t\,w)$. In the $\phi_2 = 0°$ section, the strongest maximum peak appears near the $(0\,0\,0\,1)(1\,\bar{1}\,0\,0)$ location. The other strong maximum peak appears near the $(0\,0\,0\,1)(1\,1\,\bar{2}\,0)$ position. From the $\phi_2 = 30°$ section, it can be seen that a few texture maxim appear near $(0\,0\,0\,1)[4\,\bar{3}\,1\,0]/[5\,\bar{4}\,1\,0]$ and $(0\,0\,0\,1)[1\,1\,\bar{2}\,0]$.

A summary of some important recrystallization and deformation textures formed in HCP pure metals and alloys is presented in Table 6. From these results, it might be seen that HCP metals and alloys exhibit a wider variety of recrystallization textures, which are strongly related to the initial deformation textures, annealing temperature and compositions. However, the initial deformation textures are also strongly related to the c/a ratio and the combined effects of c/a ratio and deformation mode (different slip and/or twinning modes).

4. Texture and mechanical properties relationship for hexagonal materials

Very many physical, chemical and mechanical properties of crystals depend on their crystalline orientations and it follows that directionality or anisotropy of these properties will result wherever a texture exists in polycrystalline materials. Some of the important examples are elastic modulus, Poison's ratio, strength, ductility, toughness, magnetic permeability and the energy of magnetization. These types of anisotropy apply to materials of cubic as well as lower crystal symmetry. In hexagonal metals, other properties such as thermal expansion and electrical conductivity may also show directionality. A clear treatment of these aspects of crystallography is given by Kock et al. [30]. Here only the texture strengthening and fracture behavior for hexagonal materials are included for consideration.

Engineering hexagonal materials possess fewer easy glide systems than cubic metals and alloys at room temperature, resulting in greater crystal anisotropy with more potential for texture strengthening. Although the most favored slip planes vary from metals to metals depending on the c/a ratio, the directions of easy glide are always of the type $\langle 1\,1\,\bar{2}\,0\rangle$ and therefore incapable of (or highly difficult in) producing any components of normal strain along the c-axis at room temperature. Twinning usually provides additional deformation. However, for a particular stress direction, twinning can occur only in one particular sense and, therefore, the ease of deformation in these metals depends on whether the applied stress is compressive or tensile. For example, magnesium will form twins on the $\{1\,0\,\bar{1}\,2\}\langle 1\,0\,\bar{1}\,1\rangle$ systems which allows only extension of the crystal along its c-axis. The material is therefore soft when tested in tension along this axis (with twinning) and hard in compression (without twinning). Conversely, it is strong when exposed to tensile force lying in the basal plane. So, the knowledge of active deformation modes allows us to determine the optimum conditions for texture strengthening. In extruded magnesium alloys, the $\langle 1\,0\,\bar{1}\,0\rangle$ directions are parallel to the extrusion direction, and this confers high tensile strength along the extrusion direction although with low compressive strength.

For example, the evolution of hot-working flow stress with strain was studied under the channel die compression condition in textured AZ31 magnesium alloy, including the "c-axis compression", "c-axis extension", as well as "c-axis constraint" conditions [22]. Three differently oriented channel die samples are illustrated in Fig. 15. The influence of texture can be seen in Fig. 16, which shows the compression

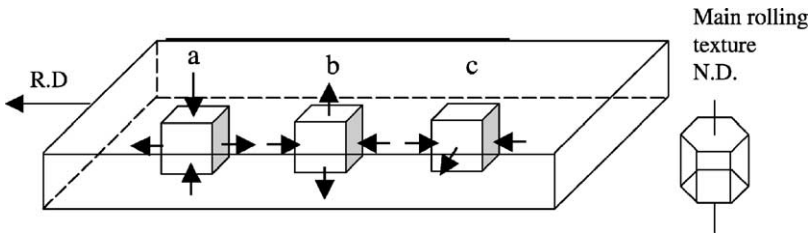

Fig. 15. Orientation of the tested AZ31 Mg samples with texture reference frame under: (a) *c*-axis compression; (b) *c*-axis extension; and (c) *c*-axis constraint.

flow curves corresponding to a temperature of 300 °C and a strain rate of 0.3 s^{-1}. The main difference of flow stress to texture at low strain is to be found in the restricted number of slip systems available in the magnesium HCP lattice. At room temperature, slip in magnesium occurs predominantly by basal slip, while prismatic and pyramidal slip become more prominent as the temperature is raised. Twinning also readily occurs on the $\{1\,0\,\bar{1}\,2\}\langle 1\,0\,\bar{1}\,1\rangle$ system. When deformation occurs in the condition of *c*-axis constraint, the prismatic $\langle a\rangle$ slip systems will be favorable in this orientation and result in the low flow stress and low strain hardening rate. When deformation occurs in the condition of *c*-axis compression, the prismatic $\langle a\rangle$ slip systems will become difficult in this orientation, and the deformation is mainly contributed by the pyramidal $\{1\,1\,\bar{2}\,2\}\langle 1\,1\,\bar{2}\,\bar{3}\rangle$ and will result in the high flow stress and high strain hardening rate. When deformation occurs in the condition of *c*-axis extension, although the prismatic $\langle a\rangle$ slip systems will be unfavorable, the pyramidal $\{1\,1\,\bar{2}\,2\}\langle 1\,1\,\bar{2}\,\bar{3}\rangle$ slip and especially twinning on the $\{1\,0\,\bar{1}\,2\}\langle 1\,0\,\bar{1}\,1\rangle$ system will bring the *c*-axis into near alignment with the plate normal. And compression will then become the predominant deformation mode, resulting in the moderate flow stress and strain hardening rate [22].

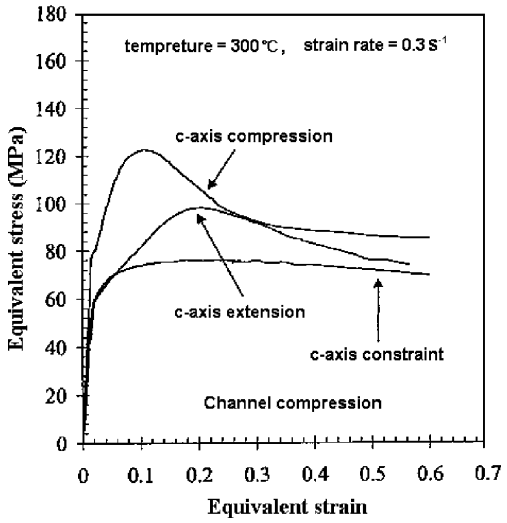

Fig. 16. Flow stress–strain curves of the AZ31 Mg alloy tensile tested at 300 °C and 0.3 s^{-1} [22].

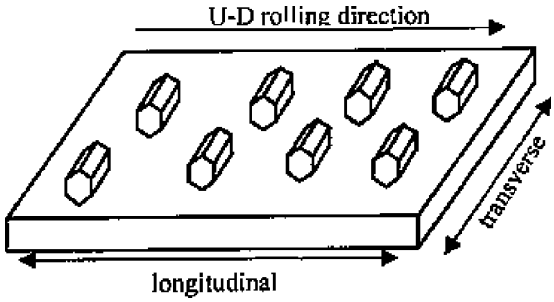

Fig. 17. Preferential orientation of the HCP crystal units in a Ti–6Al–4V plate subjected to unidirectional rolling.

The tensile and bending tests for an annealed Ti–6Al–4V alloy, with a strong macrotexture of $\{1\,1\,\bar{2}\,0\}\langle 1\,0\,\bar{1}\,0\rangle$ orientation, followed by cold rolling were performed by Bache and Evans [40]. The preferential orientation of the Ti hexagonal crystal units subjected to unidirectional rolling is shown in Fig. 17. Fig. 18 shows the stress–strain curves for the Ti–6Al–4V samples, loaded parallel to either the

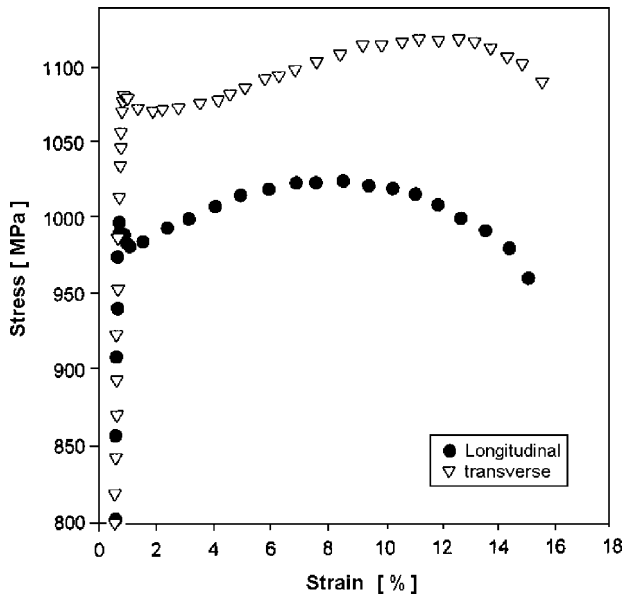

Fig. 18. Stress–strain curves for the Ti–6Al–4V samples with the tensile loading axis orientated parallel to the longitudinal and transverse directions of the rolled plate [37].

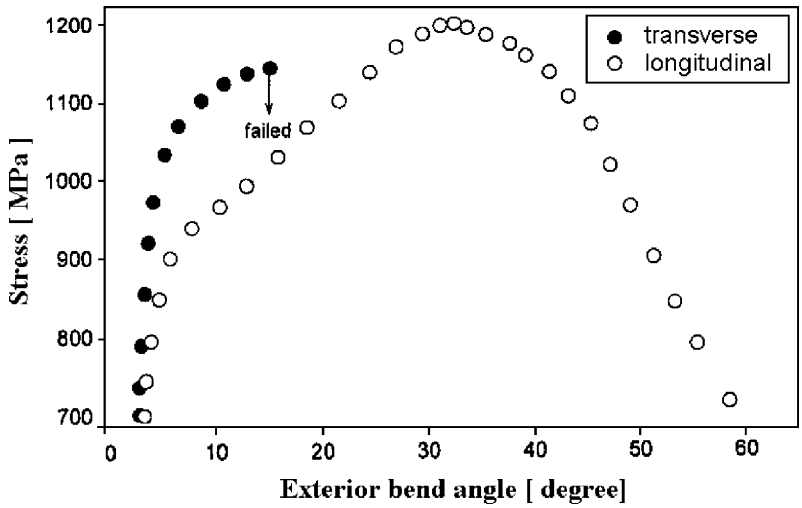

Fig. 19. Ductility bending tests for the Ti–6Al–4V beam samples with the long beam axis orientated parallel to the longitudinal and transverse directions of the rolled plate [37].

longitudinal or transverse plate orientations. The transverse sample clearly demonstrates an improved yield and ultimate tensile strength relative to the longitudinal sample. A similar relationship between strength and orientation was established under bending loading (Fig. 19) [40]. When loading parallel to transverse orientation (i.e. local tensile stress perpendicular to the L–ST plane due to bending), complete rupture was induced after ~15° of bend, whereas the longitudinal samples, stressed perpendicular to the to the L–ST plane, remained intact up to the maximum (Fig. 20). The differences in mechanical response here are consistent with the anisotropic properties demonstrated by HCP materials. These effects can be attributed to the preferential alignment of basal planes in the L–ST orientation; in such a case shear deformation and slip become highly restricted when the specimen is stressed parallel to the transverse direction. In contrast, slip will be more easily accommodated in the longitudinal samples, since the prismatic ⟨*a*⟩ slip system of the HCP units in Ti will be more favorably inclined to the tensile axis.

Also, the texture affects the fracture behavior because the crystallography orientation has a close relationship with the crack path. For example, this has been demonstrated by the Charpy impact results shown in Fig. 21 for a textured Ti alloy tested in two different directions [39]. The preferred orientation of the alloy was centered on the component $\{1\,1\,\bar{2}\,0\}\langle 1\,\bar{1}\,0\,0\rangle$. The cleavage fracture energy and transition temperature are very different. Its influence can be ascribed to the level of stress that develops at the tip of the notch or crack. If the preferred orientation is such that the slip systems around the crack tip are easily activated, then plasticity rather than fracture is favored and high toughness results. Conversely, if plastic flow is difficult to proceed,

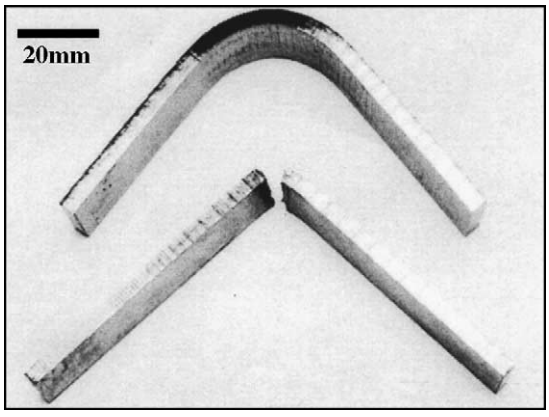

Fig. 20. The Ti–6Al–4V specimens after bending tests with the long beam axis parallel to the longitudinal (top) and transverse (bottom) directions of the rolled plate [37].

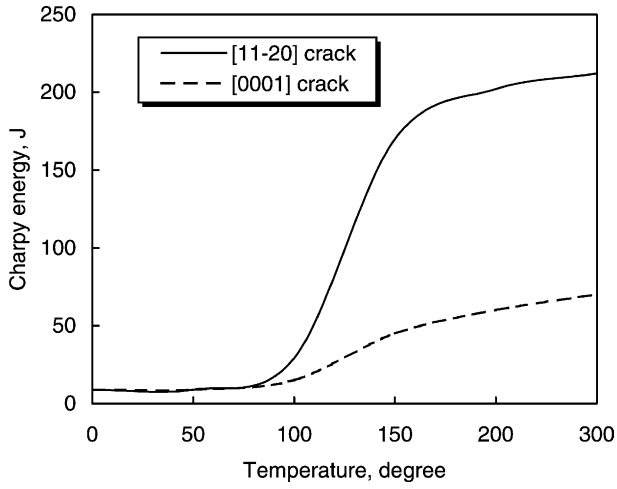

Fig. 21. Temperature dependence of the Charpy energy for textured Ti samples taken from the rolling direction of a rolled plate. The existing texture caused the variation of toughness energy depending on the direction of crack propagation [40].

then a state of high stress is generated at the crack tip and fracture occurs.

5. Conclusion

The main characters of deformation texture in hexagonal materials with different c/a ratios are crudely classified into three groups. The tendency is that (i) the basal $\{0\,0\,0\,1\}\langle 1\,1\,\bar{2}\,0\rangle$ slip will result in the basal texture for Mg ($c/a \approx 1.633$); (ii) the combination of basal $\{0\,0\,0\,1\}\langle 1\,1\,\bar{2}\,0\rangle$ slip and pyramidal $\{1\,1\,\bar{2}\,\bar{2}\}\langle 1\,1\,\bar{2}\,3\rangle$ slip will result in the textures with basal poles tilted away from the normal direction toward the rolling direction for Zn or Cd ($c/a > 1.633$); and (iii) the combination of prismatic $\{1\,0\,\bar{1}\,0\}\langle 1\,1\,\bar{2}\,0\rangle$ slip and basal $\{0\,0\,0\,1\}\langle 1\,1\,\bar{2}\,0\rangle$ slip will result in the textures with basal poles tilted away from the normal direction toward the transverse direction for Ti and Zr ($c/a < 1.633$). This is mainly contributed by the activation of different slip systems under different deformation modes. Also, the texture will affect the mechanical properties because the crystallography orientation has a significant relationship to slip and twining systems which corresponding to the deformation modes. Texture strengthening and texture toughening in hexagonal materials have been observed in hexagonal metals, a similar effect as those observed in cubic materials.

Acknowledgements

The authors would like to gratefully acknowledge the sponsorship from National Science Council of ROC under the projects NSC 89-2216-E-110-043 and NSC 90-2216-E-110-024. The author Y.N. Wang is grateful to the post-doc sponsorship from NSC under the contrast NSC 90-2816-E-110-0001-6.

References

[1] P. Echlin, C.E. Fiori, J.I. Goldstein, D.C. Joy, C.E. Lyman, E. Lifshin, D.E. Newbury, A.D. Romig, Scanning Electron Microscopy and X-ray Microanalysis, Plenum Press, London, 1992.
[2] C. Escher, G. Gottstein, Acta Mater. 46 (1998) 525.
[3] I.C. Hsiao, S.W. Su, J.C. Huang, Metall. Mater. Trans. 31A (2000) 2169.
[4] T.R. McNelley, D.L. Swisher, M.T. Perez-Prado, Metall. Mater. Trans. 33 (2002) 279.
[5] X. Huang, Scr. Mater. 38 (1998) 1697.
[6] K. Sztwertnia, F. Haessner, Mater. Sci. Forum 157–162 (1994) 1291.
[7] G.C. Kaschner, G.T. Gray, Metall. Mater. Trans. 31A (2000) 1097.
[8] J.J. Fundenberger, M.J. Philippe, F. Wanger, C. Esling, Acta Mater. 45 (1997) 4041.
[9] N. Gey, M. Humbert, Acta Mater. 50 (2002) 277.
[10] S.L. Semiatin, T.R. Bieler, Metall. Mater. Trans. 32A (2001) 1801.
[11] F. Wanger, N. Bozzolo, O. Van Landutyt, T. Grosdidier, Acta Mater. 50 (2002) 1245.
[12] S. Suwas, R.K. Ray, A.K. Singh, S. Bhargava, Acta Mater. 47 (1999) 4585.
[13] S. Suwas, R.K. Ray, Scr. Mater. 44 (2001) 275.
[14] S. Suwas, R.K. Ray, Metall. Mater. Trans. 31A (2000) 2339.
[15] S.L. Seniatin, P.N. Fagin, M.G. Glavicic, I.M. Sukonnik, O.M. Ivasishin, Mater. Sci. Eng. A 299 (2001) 225.
[16] S.V. Divinski, V.N. Dnieprenko, O.M. Ivasishin, Mater. Sci. Eng. A 243 (1998) 201.
[17] T. Mukai, M. Yamanoi, H. Watanabe, K. Higashi, Scr. Mater. 45 (2002) 89.
[18] S.F. Su, J.C. Huang, H.K. Lin, N.J. Ho, Metall. Mater. Trans. 33A (2002) 1461.
[19] D.J. Bacon, V. Vitek, Metall. Mater. Trans. 33A (2002) 721.
[20] S.R. Agnew, M.H. Yoo, C.N. Tome, Acta Mater. 49 (2001) 4277.
[21] P. Klimanek, A. Potzsch, Mater. Sci. Eng. A 324 (2002) 145.
[22] M.R. Barnett, J. Light Metals 1 (2001) 167.
[23] T. Mohri, M. Mabuchi, M. Nakamura, T. Asahina, H. Iwasaki, T. Aizawa, K. Higashi, Mater. Sci. Eng. A 290 (2000) 139.
[24] M.T. Perez-Prodo, O.A. Ruano, Scr. Mater. 45 (2001) 89.
[25] M. Suzuki, H. Sato, K. Maruyama, H. Oikawa, Mater. Sci. Eng. A 319–321 (2000) 751.
[26] M. Regev, A. Rosen, M. Bamberger, Metall. Mater. Trans. 32A (2001) 1335.
[27] O.A. Lambri, W. Riehemann, Z. Trojanova, Scr. Mater. 45 (2001) 1365.
[28] K. Mathis, Z. Trojanova, P. Lukac, Mater. Sci. Eng. A 324 (2002) 141.
[29] H.J. Bunge, Texture Analysis in Materials Science, Butterworths Press, London, 1982.
[30] U.F. Kock, C.N. Tome, H.R. Wenk, Texture and Anisotropy: Preferred Orientation in Polycrystals and Their Effect on Materials Properties, Cambridge University Press, Cambridge, 1998.
[31] L.G. Schulz, J. Appl. Phys. 20 (1949) 1030.
[32] M.E. Schlienger, J.T. Stanley, H.L. Fraser, Commercial Software Diffract 1.2a, Macintosh Version, Microdev Software Company, Evergreen, CO, USA.
[33] C. Boudias, D. Monceau, Commercial Software CaRIne Crystallography 3.1, Divergent SA Company, Compiegne, France.
[34] R.J. Roe, J. Appl. Phys. 36 (1965) 2024.
[35] H.J. Bunge, Z. Metallkd. 56 (1965) 872.
[36] R.E. Reed-Hill, R. Abbaschian, Physical Metallurgy Principles, third ed., PWS-KENT Publishing Co., Boston, 1992, p. 546.
[37] O. Engler, Metall. Mater. Trans. 30A (1999) 1517.
[38] F.J. Humphreys, P.N. Kalu, Textures Microstruct. 14–18 (1990) 703.
[39] M. Hatherly, W.B. Hutchinson, An Introduction to Textures in Metals, Chameleon Press, London, 1990.
[40] M.R. Bache, W.J. Evans, Mater. Sci. Eng. A 319–321 (2001) 409.